# Indirect measurement of the shrinkage forces acting during the drying of a paper coating layer.

**G.M. Laudone[†], G.P. Matthews[†*] and P.A.C. Gane[§]**

[†]*Environmental and Fluid Modelling Group, University of Plymouth,*

*Plymouth PL4 8AA, UK.*

*§ Omya AG, CH-4665 Oftringen, Switzerland.*

## Abstract

A coated paper consists of a mineral coating (e.g. clay, calcium carbonate, titanium dioxide or silica) containing a binder (e.g. starch, proteins or latex) to fix it to the fibrous paper substrate. The coating is applied to the paper surface as a slurry. The shrinkage occurring while the coating layer dries has been measured by observing the deflection of strips of a substrate coated with calcium carbonate and different binders. The force acting on the surface of the strips to cause a given deflection has been calculated using the Elementary Beam Theory. The porous structure generated by the dry coating layer has been studied using mercury porosimetry and Pore-Cor, a software package able to generate a model network structure of porous materials using data derived from mercury porosimetry.

* To whom correspondence should be addressed.
Tel. and fax: +44 1752 233021
Email: pmatthews@plymouth.ac.uk

Within this simulated structure, both the water distribution during drying and the dynamic wetting can be studied spatially in a virtual reality environment. The experiments and simulation provide a better understanding of these processes which, together with the polymeric binder film forming behaviour, are considered responsible for the shrinkage of the coating layer.

**Keywords:** Paper coating, binder film formation, shrinkage, drying of porous structures, capillary force modelling, dynamic wetting.

---

# 1. Introduction

The market demand and consequent production of coated paper, used in products such as "glossy" magazines, advertising, art papers and packaging, is rapidly increasing. The natural consequence of such a growth in this market is the increasing interest for new developments and a better understanding of the basic processes of this production, in particular with respect to the effect of surface uniformity on print performance. The application of a pigmented coating layer to a base sheet of paper or board improves its optical and printing properties such as uniformity in appearance, gloss or matt finish, opacity, ink absorption with controlled ink spread etc., and gives enough capillarity to allow ink setting within the time-scale of a modern printing press.

A coating colour formulation typically consists of:

- *water*: the coating is applied as an aqueous particulate suspension;
- *pigments*: amongst others calcium carbonate (ground or precipitated), clays, polymeric pigments, titanium dioxide, silica or talc can be used;
- *binders*: needed to provide good cohesion of the porous structure formed by

pigments and adhesion of the coating to the substrate.

The usual composition of a coating colour formulation on a dry basis is 80-90 w/w% mineral pigment and 10-20 w/w% binder. The solid content in the water dispersion is usually between 50 and 70 w/w%. Other compounds, such as dispersants, are used in the formulation of the coating colour in lower percentages to act as stabilising agents and to make the components compatible in water suspensions. The particle diameters for the mineral pigments usually range from 0.01 to 10 μm. A thin layer (5 – 10 μm) of coating colour formulation is metered on the surface of the base-paper and is dried thermally.

The binders are usually divided into two types: natural (like starch or protein) and synthetic (like styrene-butadiene, styrene-acrylic latex, or poly(vinyl acetate)). The natural binders often give poor results in terms of gloss and light scattering, partly due to the coating shrinkage during film-forming upon drying. Synthetic binders suffer less from this problem, and their use, as a result, is becoming more popular in the coated paper industry.

Attempts to follow the process of consolidation of the coating layer have been made by various authors using several different techniques [1-5]. They all follow the initial approach proposed by Watanabe and Lepoutre [1], who divided the drying process into three stages. The application of the coating is followed by a first phase of water evaporation at the liquid-air interface. This phase is unaffected by the solid content in the liquid phase. At the *first critical concentration* (FCC), a three-dimensional network is formed and particle motion is greatly restricted. The water-air interfaces recede into the surface capillaries, creating a capillary pressure that causes a shrinkage of the network.

This continues until the *second critical concentration* (SCC) is reached, at which the network is fixed and air enters the rigid structure.

Practically little is known about the distribution of the liquid-air menisci in a porous network undergoing drying, and especially the forces related to the capillarity acting at the free liquid front. The role of these forces in combination with the film forming and compressibility characteristics of the binders has not previously been addressed. The evaporation, however, of a liquid from a porous medium has been studied with an interesting approach by Laurindo and Prat [6-8]. They studied evaporation as a displacement between two immiscible fluids. As evaporation results in the invasion of the porous media by a non-wetting phase (vapour), the similarity with percolation is evident. They created a bi-dimensional network model describing isothermal evaporation, controlled mainly by mass transfer, as they considered the effect of the heat transfer to be negligible in their experimental conditions. They also considered the viscous forces to be negligible upon drying. The latter approximation is acceptable if the evaporation is slow, and/or if the length of pore features is short, i.e. the aspect ratio of the pores is low, as is the case with isotropic calcite particles.

Our aim was to reach a better understanding of the shrinkage phenomena which occurred during drying. This was achieved by considering the relative importance of the capillary forces acting on the coating colour formulation while the water receded into the porous structure formed by the pigment particles, and the shrinkage force of the film-forming binders/polymers.

The dry samples were analysed with mercury intrusion porosimetry and their porous structures were modelled with a network simulation software. The future aim of

the study is to determine the distribution and areas of the free menisci in the porous structure. This will allow the calculation of the meniscus forces as the derivative of the total free energy of the liquid-mediated interface (Gao [9]; Gao et al. [10]). These calculated forces will then be compared with those observed experimentally.

# 2. Experimental

## *2.1. Method and materials*

The characterisation of the forces acting during the drying of the thin coating layer applied onto paper cannot be carried out directly. This is due to the complexity and small dimensions of the system. Thus it is necessary to find an indirect approach. Therefore, we decided to measure such forces by observing the deflection of an elastic material upon drying. Many different materials, mainly polymeric films, were tested and Synteape[1], a synthetic laminate substrate made from a stretched calcium carbonate-filled polypropylene (fig.1), was chosen. Its elastic behaviour and its slightly rough surface, able to "accept" the coating colour formulation, made it the ideal substrate for our experiment. The precise formulation and preparation method of Synteape is a trade secret. It is possible to apply the coating layer, allow it to dry progressively and measure the deformation of the Synteape as a function of time, and hence as a function of solids concentration.

[1] Synteape is a product name of Arjo Wiggins, Issy Le Moulineaux, France.

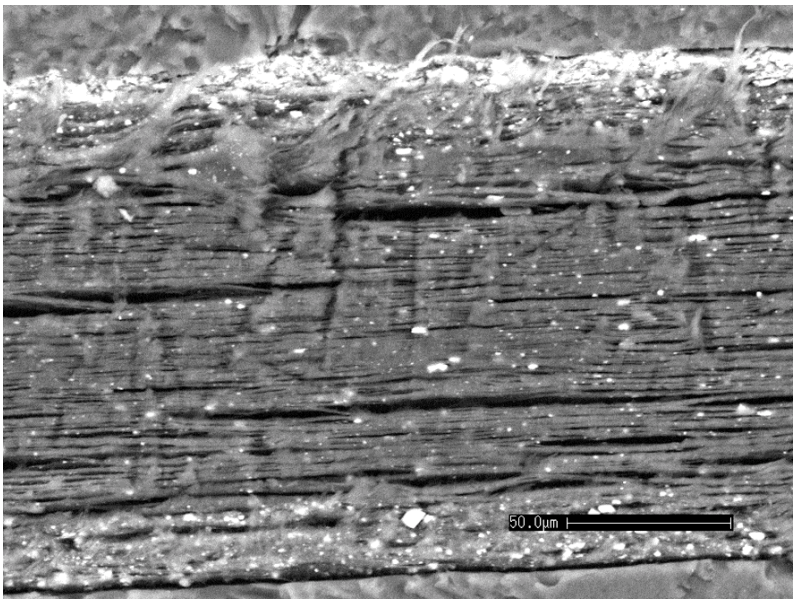


**Figure 1 – SEM micrograph of the cross section of Synteape showing the laminated structure and $CaCO_3$ particles. Scale bar 50 µm**

By approximating a strip of Synteape to an elastic bending beam, it is possible to use the standard theory (as detailed in the Appendix) which relates the forces acting on the beam with the actual deflection of the beam itself. The forces acting on the surface, causing the deformation, can thus be calculated through the *Young's modulus* of the Synteape.

It is not possible to derive these forces from coatings on a fibrous paper substrate because paper has a plastic response behaviour: its fibres, under the forces caused by the drying coating layer, rearrange, especially under high moisture conditions. This rearrangement causes a deformation in the plane of the paper displaying no measurable bending other than the action of wetting on the built-in stress relaxation properties of the fibre mat formation. This planar deformation, however, cannot act to alleviate the non-uniformities of the coating caused by the shrinkage phenomenon.

In this kind of approach we made three main assumptions:

- the weight of the beam was negligible when compared with the forces acting on its surface, the Synteape strip being 4.5 cm long, 0.5 cm wide and 0.01 cm thick;
- the weight of the strip was assumed to be negligible when compared with the shrinkage forces;
- the mechanical properties of the system did not change during the drying of the coating layer, which means that we considered the coating layer just like a *stress deliverer*.

The mechanical properties of the Synteape are realistically assumed to be elastic and acting within the Hookean elastic limit. However, the coating laminate layer does change properties from plastic, through a viscoelastic structure to a brittle structure as drying proceeds. These changes, however, relate to the effective deformation and indeed contribute to the mechanical behaviour of the system. Therefore, the exact mechanical transitions between these states of the coating are not the target of investigation, rather the roles of the various force components as a function of time and concentration which lead to the transitions.

Taking several pictures of the sample during the drying process and measuring its weight loss during the process makes it possible to find the forces acting on the surface of the substrate as a function of weight (water) loss. A diagram of the experimental apparatus is presented in fig.2. In order to understand which part of the shrinkage forces is due to the capillary forces only and which is due to other effects, such as the shrinkage of the drying binder, it was necessary to create different structures, which would mimic and separate individual components of the combined force process. These consisted of:

- pigment and stabilisers only (capillary forces acting only during the drying);
- complete coating formulations with pigment and binders.

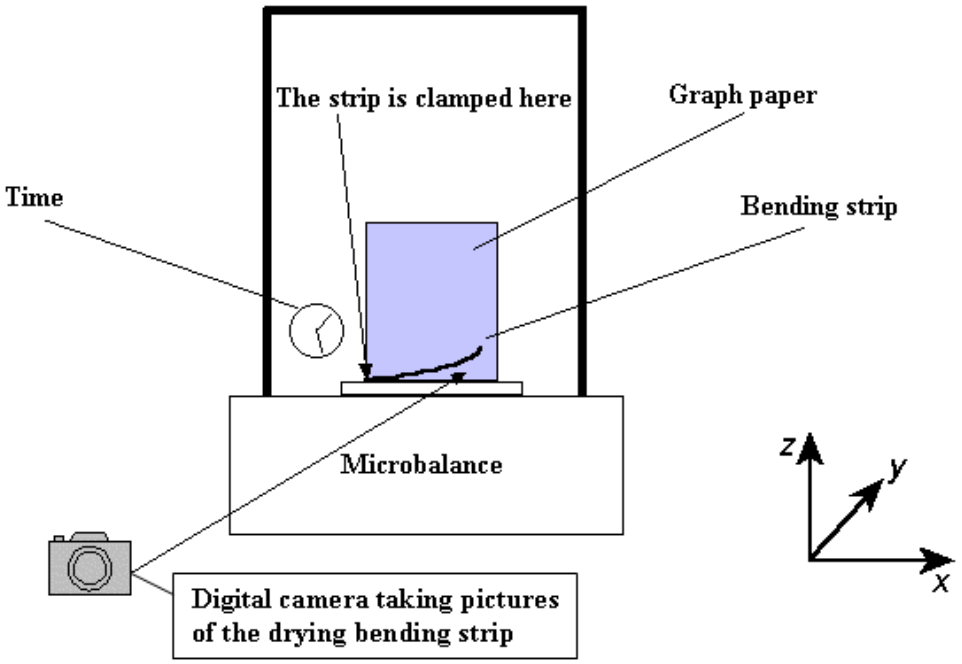


**Figure 2 –Diagram of the experimental apparatus for the indirect measurement of the shrinkage forces**

## *2.2. Formulation components*

The method described above makes it possible to measure the forces that drying pigmented structures exert on the surface of the elastic substrate. The different coatings used in these experiments are based on Ground Calcium Carbonate (GCC), to avoid the problems presented by the anisotropy of clay platelets and the acicularity of aragonitic Precipitated Calcium Carbonate (PCC). Adsorption of starch [11-12] onto clay together with particle anisotropy lead to poorly definable orientation effects. PCC, even if calcitic forms are chosen, has a narrow size distribution and thus results in a highly packed structure which acts to reduce the measurable capillary effects, and, in reality, the permeability of PCC coatings dominates the fluid drainage on real paper: this, in turn, would tend to negate the relevance of the study using the non-permeable synthetic base

material. Therefore, Hydrocarb[2] 90 (HC90OG), a dispersed GCC limestone from Orgon, France, with 90 w/w% of particles having a diameter < 2 μm, was chosen for the preparation of our samples.

The different behaviours of natural and synthetic binders was studied by preparing different coating colour formulations based on:

- maize starch C-film 07321[3]
- high glass transition temperature ($T_g$ = 23 °C) acrylic latex Acronal S320D[4] and
- low glass transition temperature ($T_g$ = 5 °C) styrene butadiene latex DL930[5].

The choice of latex binders was based on the study of offset coating formulations. Offset printing demands high binding power and control of permeability. The use of different latices of high and low $T_g$ covers these respective demands. The impact of the chemical structures of the synthetic binders on coating structure is assumed to be negligible as both latex types are designed for stability in the presence of calcium ions.

On a dry basis, the composition of our coating colour formulations was 25 w/w% binder and 75 w/w% pigment. This is a higher percentage of binder than in a typical industrial paper coating, but the level was chosen in order to maximise the effect of the binder shrinkage in the following observations. A preliminary series of experiments showed that the effect of binder was proportional to its content within this dosage range, and so the increased binder quantity is a useful experimental parameter to employ without influencing the basic mechanisms themselves.

[2] Hydrocarb is a product name of Omya AG, Oftringen, Switzerland
[3] C-film is a product name of Cerestar, France
[4] Acronal is a product name of BASF, Ludwigshafen, Germany
[5] DL930 is a product name of Dow Chemical, Midland, MI USA

In order to investigate the effect of the amount of coating colour formulation applied, the strips were coated using two different draw-down coating rods. These rods have a wire winding applied to the surface to define a given application volume in contact with the substrate. The diameter of the wire winding controls this volume. The rods were labelled "rod 2" (applying about 10 g/m$^2$ of dry coating corresponding to a dry coating layer thickness of about 5μm) and "rod 3" (applying about 20 g/m$^2$ of dry coating, corresponding to a dry coating layer thickness of about 10 μm).

## *2.3. Mercury porosimetry*

Mercury porosimetry has been used for the characterisation of the porous structure formed by the dried coating [13-14]. An evacuated sample is immersed in mercury, and the external pressure is gradually increased. The amount of mercury intruding the void space of the sample is measured as a function of pressure: the amount increases as the pressure increases and the mercury is forced into smaller voids. The result is a mercury intrusion curve, which, knowing the interfacial tension and contact angle of mercury with the solid, can be converted into a void size distribution by the Laplace equation, assuming that the structure consists of equivalent capillary elements of diameter $D$:

$$D = \frac{-4\gamma \cos\theta}{P} \qquad (1)$$

where $\gamma$ is the interfacial tension between mercury and air (0.485 N/m), $P$ is the applied pressure and $\theta$ is the contact angle. A similar procedure with pressure reduction allows the drainage curve to be obtained as the mercury emerges from the sample. The intrusion and extrusion curves differ and show hysteresis caused by the pressure needed to force the mercury into a larger void space (pore) through a narrower void space (throat) being

greater than that at which it will come out when the pressure is decreasing, i.e. small throats can shield large pores.

Mercury porosimetry can be used to determine the pore size distribution of porous materials even when these are supported by a laminate or fibrous substrate. The technique described by Ridgway and Gane [15] makes it possible to correct the results of the mercury porosimetry in order to subtract the contribution of the substrate.

The mercury porosimetry tests made on our dry samples were carried out using a Micromeritics Autopore III mercury porosimeter, able to reach a pressure of 414 MPa.

## *2.4. Modelling*

### 2.4.1. Pore-Comp

Pore-Comp[6] is a precursor software for Pore-Cor[7]. It corrects the mercury intrusion curves for:

- mercury compression and penetrometer expansion;
- compressibility of skeletal solid phase of the sample.

The correction for the compression of mercury, expansion of the penetrometer and compressibility of the solid phase of the sample is calculated using the following equation from Gane et al. [16]:

$$V_{\text{int}} = V_{\text{obs}} - \delta V_{\text{blank}} + \left[ 0.175(V^1_{\text{bulk}}) \log_{10}\left(1 + \frac{P}{1820}\right)\right] - V^1_{\text{bulk}}(1-\Phi^1)\left(1 - \exp\left[\frac{(P^1 - P)}{M_{\text{ss}}}\right]\right) \quad (2)$$

$V_{\text{int}}$ is the corrected volume of mercury intruded into the sample, $V_{\text{obs}}$ the experimentally observed volume of intruded mercury, $\delta V_{\text{blank}}$ the change in the blank run volume

[6-7] Pore-Comp and Pore-Cor are software names of the Environmental and Fluids Modelling Group, University of Plymouth, U.K

reading, $V^1_{bulk}$ the sample bulk volume at atmospheric pressure, $P$ the applied pressure, $\Phi^1$ the porosity at atmospheric pressure, $P^1$ the atmospheric pressure and $M_{ss}$ the bulk modulus of the solid sample.

### 2.4.2. Pore-Cor

The Pore-Cor model [17-19] simulates the pore-level properties of a porous medium. It generates a three-dimensional structure, consisting of a repeated unit cell containing a regular 10x10x10 array of cubic pores interconnected by cylindrical throats, which matches the experimentally determined porosity and void size distribution, such that the percolation characteristics measured by mercury porosimetry are reproduced. The simulation is performed by optimising sets of adjustable parameters, such as connectivity, pore and throat skew - each affecting, in turn, the relevant size distribution. More than one structure can be generated by the model to fit an experimental intrusion curve since the pores in a modelled unit cell can be arranged in different ways. This creates simulated pore structures with different best-fit values of the adjustable parameters. The model creates different families of structures called "stochastic generations". Each stochastic generation is created by using a different set of pseudo-random starting numbers. If the unit cell is the same size as the Representative Elementary Volume (REV) of the sample, and its complexity is equivalent to the complexity of the experimental void structure, then different stochastic generations will have the same properties, as the random effects will average out across the unit cell. Frequently, however, the unit cell is smaller than the REV of the sample. In this case the problem can be overcome by studying the properties of different stochastic generations, but this is outside the scope of this work.

Pore-Cor was used to generate the following simulated measurements: throat and pore-size distribution, fluid and gas absolute permeabilities, connectivity and dynamic liquid absorption measurements.

Using the Virtual Reality Mark-up Language, Pore Cor was used to generate simulated structures in a virtual reality environment. These can be explored at the web page www.pore-cor.com/virtual_reality.com

## 3. Results and discussion

### *3.1. Bending strips*

A detailed image analysis of the bending beam viewed in the *xz* plane (fig.2) and the application of the software package *Table Curve 2D* [8] made it possible to confirm the initial hypothesis of circular deformation of the strips and the negligibility of the weight of the samples.

The stiffness of the beam *EI* (as defined in the Appendix) was calculated for the Synteape substrate, and data were collected from the microbalance as the curling of the samples was measured. The value of $\tau$ (written tau in the figures), which is the force per unit of area within the cross section of the coating, was plotted as a function of the weight loss. $\tau$ is equal to *T* (as defined in the Appendix) divided by the surface area of the coated strips.

[8] Table Curve 2D is a software program of SPSS Inc., 444 North Michigan Avenue, Chicago, IL 60611, USA

The results are shown in figs.3-6, where the continuous lines represent the samples coated with a lower weight of coating per unit of surface and the dotted ones represent the samples coated with a higher weight of coating per unit of surface.

There is no information available for the samples coated with $CaCO_3$ slurry alone using rod 2 because the bending of the strip and the following relaxation was too rapid to be observed with the technique used. Fig.3, therefore, does not show any continuous line.

From fig.3 it is possible to observe the effect of the capillary forces only acting upon drying, i.e. in the absence of binder. The samples bend as soon as the drying begins and the water recedes into the porous structure created by the particles of calcium carbonate, reaching a peak of about 50-60 Pa. The more the water leaves the structure the weaker are the capillary forces. This leads to a complete relaxation of the sample with no stress retention at all. This case of the purely meniscus-driven deformation, which disappears on complete drying, provides the control experiment. The effect of the presence of binder in the coating colour formulation can be observed by comparing the results from the control experiment with the results obtained when complete coating colour formulations were used.

It is interesting to notice (fig.4) how hard, high $T_g$, latex-based samples show almost no deflection. The maximum stress measured on these samples is 10 Pa, lower than that measured on the samples coated with $CaCO_3$ only. It appears that this kind of latex acts to fill the structure but the spheres are non-deformable and so shrinkage cannot occur even by the capillary forces.

Soft, low $T_g$ latex (fig.5) allows such deformation and the capillary forces act causing deflection of the strip. The fixation of the capillary-induced structure takes place where the binder is present in the structure. The binder allows the deformation to take place and serves to hold the deformation during the adhesional bonding between itself and the pigment particles.

The force acting while a starch-based coating colour formulation is drying is far larger (fig.6) than in the case of latex-containing formulations, although the results for this formulation are more scattered. Inclusion of starch acts to flocculate the pigment due to partial adsorption of starch onto the $CaCO_3$ particles and osmotic effect. This reduces the effective number of voids in the dried coating but simultaneously tends to make those that are present larger. The unit size for flocculated pigment and starch is close to that of the layer thickness for rod 2 and slightly smaller for rod 3, i.e. the effective particle size in relation to film thickness is an important parameter when considering the rearrangement ability of the particles in the layer undergoing shrinkage. A slight upward gradient of the force curve as the coating dries indicates a real shrinkage force originating from starch film formation.

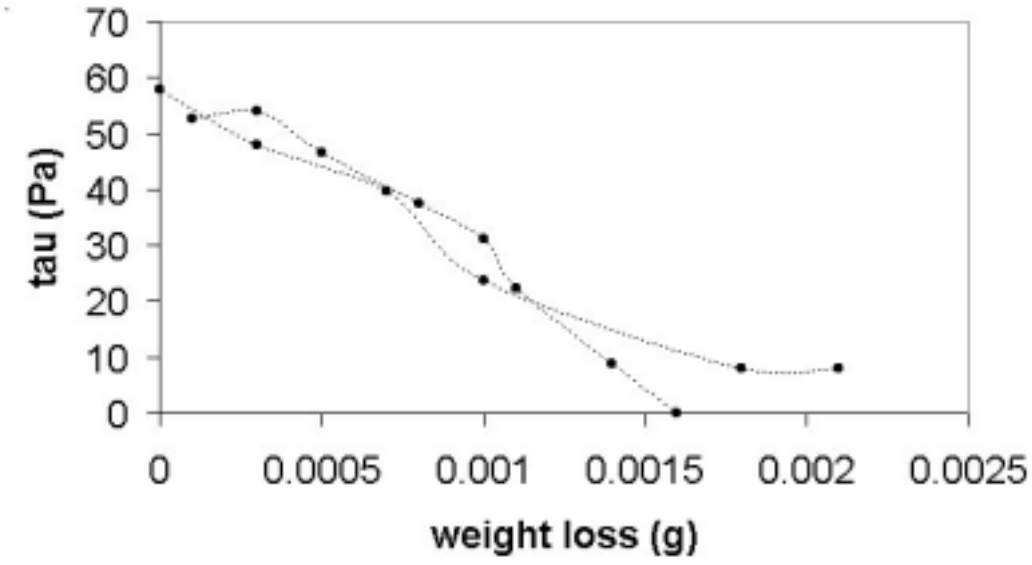


**Figure 3 - Stress acting on two replicate samples coated with calcium carbonate only. The maximum stress measured is 58 Pa.**

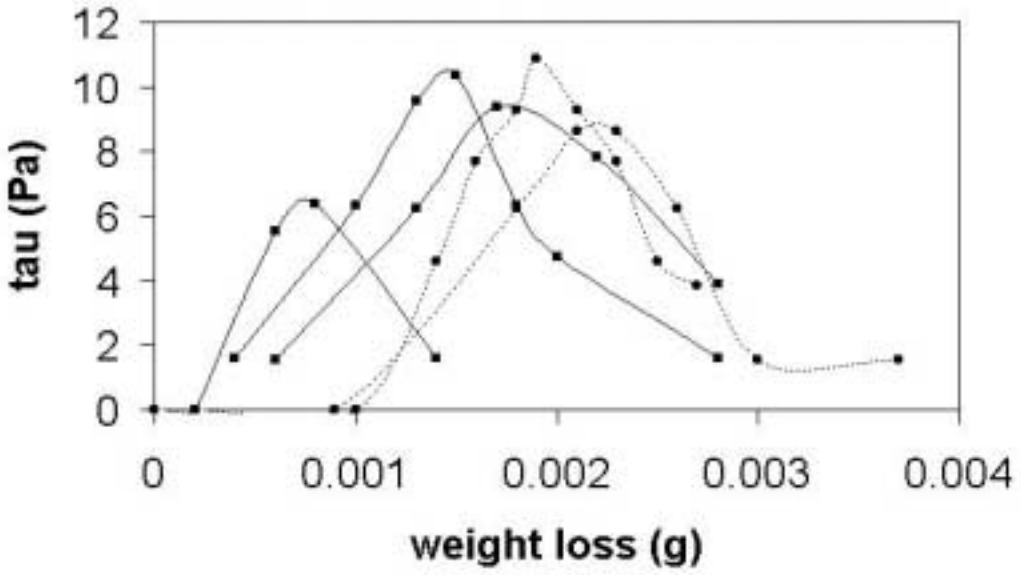


**Figure 4 - Stress acting on samples coated with a high $T_g$ latex-based coating colour formulation. The continuous lines represent the samples coated with rod 2, while the dotted ones represent rod 3. The maximum stress measured is lower than in the case of $CaCO_3$ slurry with no binder.**

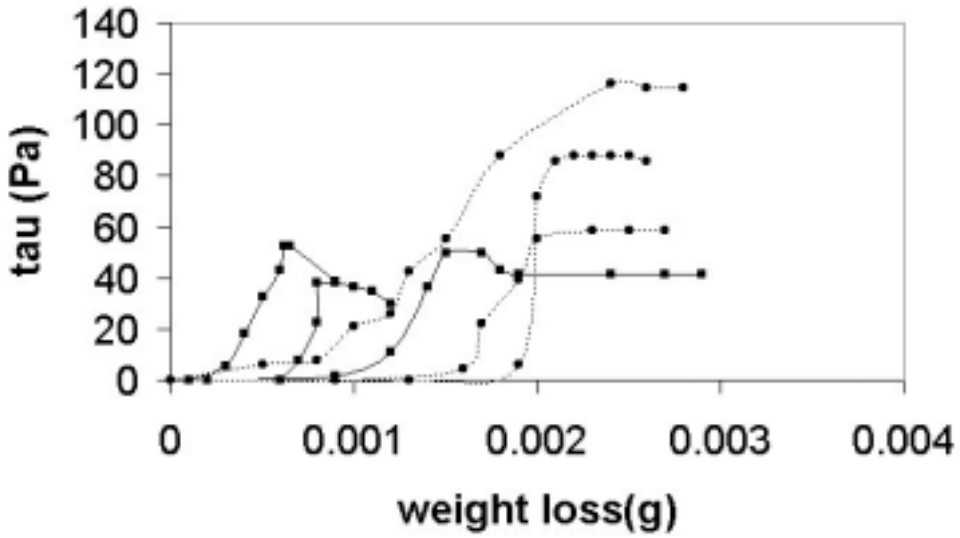


**Figure 5 - Stress acting on samples coated with a low $T_g$ latex-based coating colour formulation. The continuous lines represent the samples coated with rod 2, while the dotted ones represent rod 3. The stress measured is larger than in the case of $CaCO_3$ slurry only and part of the stress is retained by the binding action of the latex.**

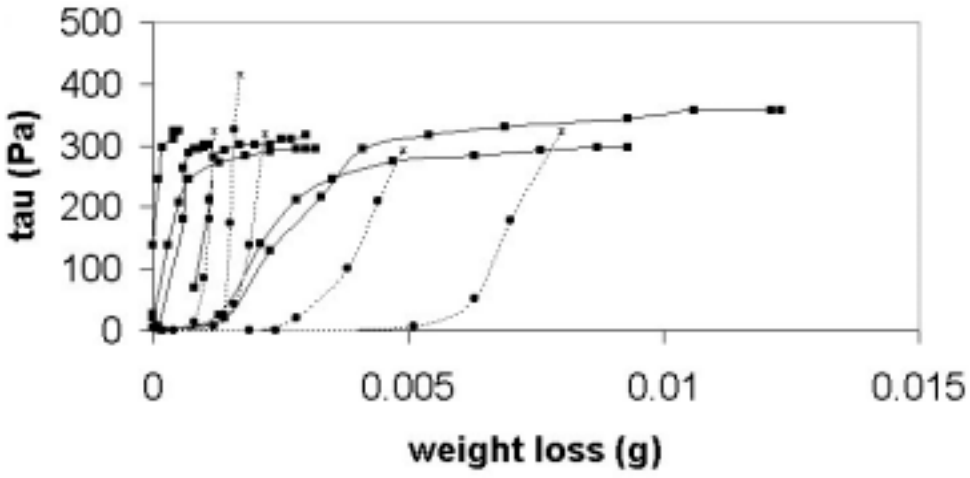


**Figure 6 - Stress acting on samples coated with a starch-based coating colour formulation. The continuous lines represent the samples coated with rod 2, while the dotted ones represent rod 3. The stress measured is far larger than in the case of latex-based coating colour formulations.**

To confirm such interpretation it is necessary to characterise the porous structure created by the drying coating colour formulation using mercury porosimetry and model the porous structure using Pore-Cor.

## *3.2. Mercury porosimetry*

A series of dry samples coated with the same coating colour formulations used for the preparation of the bending strips were analysed with the mercury porosimetry technique.

The results of the mercury porosimetry on the dried samples were first corrected with the use of Pore-Comp. The correction of the intrusion curves for the compressibility of the mercury and the expansion of the glass chamber at high pressure and for the compressibility of the sample itself led to the following values (Table 1) of fully corrected porosity:

**Table 1- Fully corrected porosities (%)**

| low $T_g$ latex rod 2 | low $T_g$ latex rod 3 | high $T_g$ latex rod 2 | high $T_g$ latex rod 3 | starch rod2 | starch rod 3 |
|---|---|---|---|---|---|
| 21.0 | 30.8 | 29.2 | 18.9 | 13.5 | 16.3 |

In fig.7 the results of the mercury porosimetry are presented. The intrusion curves for the starch-based samples confirm the interpretation given in the previous section: the starch-based samples show a lower porosity but bigger pores (especially the coating applied with rod 2), suggesting that the flocculating action of the starch causes the aggregation of the pigment itself, making the structure more permeable with bigger pores but having lower overall porosity. This can be visually confirmed by the electron microscopy image for a starch-based sample, shown in fig.8. It is clear from such a picture that there is the presence of big pores at the surface of the coating layer. This phenomenon explains also the bimodality of the intrusion curves for starch-based coating colour formulations.

It is interesting to notice the trend in the values of porosity: the samples most prone to shrinkage can be placed in the order: starch > low $T_g$ latex > high $T_g$ latex. The most shrinkage is expected (and observed in the case of starch and low $T_g$ latex) from a higher coating weight, but this does not always lead to a lower porosity as would be

intuitively expected. Both low $T_g$ latex- and starch-based coating colour formulations show a higher porosity for increasing amount of coating colour formulation applied onto the surface. This can be explained in terms of the presence of a "mud cracking" effect on the surface of *shrinking* binder-based coating formulation at higher weight of coating per unit of surface applied. This is represented by the slight bimodality shown in the intrusion curve for the low $T_g$ latex applied with rod 3. The presence of "mud cracks" on the surface of the coating layer can be observed in fig.9.

The high $T_g$ latex-based coatings, however, do follow the expected trend in respect to decreasing porosity as a function of coating weight. High $T_g$ latex samples do not manifest shrinkage, and the "mud cracking" effect is not present on such non-shrinking samples.

The coating colour formulations prepared using high $T_g$ latex show significant intrusion for pore diameters of $\sim 0.2$ μm and smaller. The latex particles have a diameter of $\sim 0.15$ μm. Thus we can suggest why the samples coated with these coating colour formulations do not bend while the coating dries: the hard and non-deformable particles of high $T_g$ latex fill the porous structure formed by the calcium carbonate, making it impossible for the capillary forces to cause deformation and shrinkage.

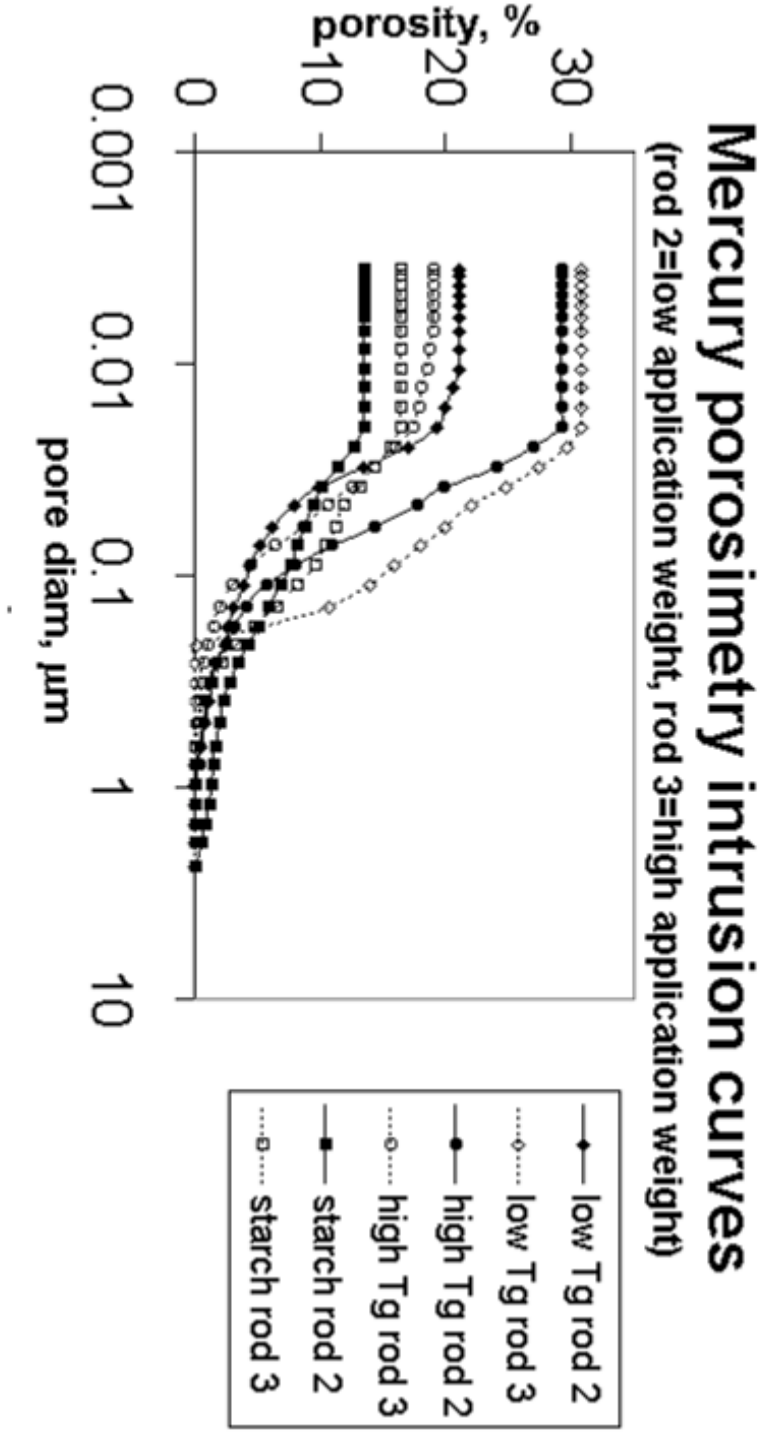


**Figure 7 - Mercury porosimetry intrusion curves**

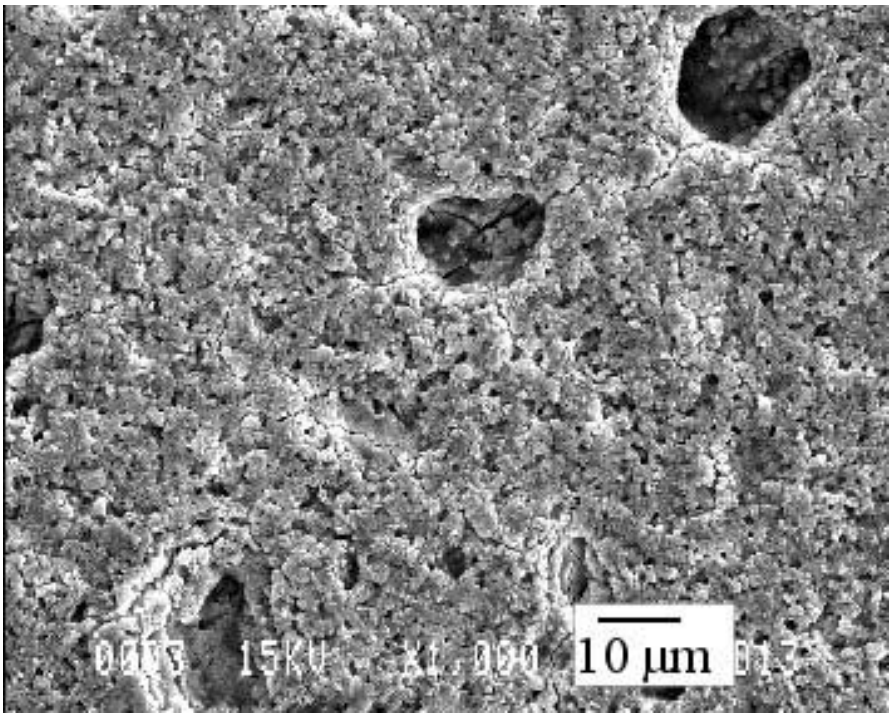


**Figure 8 – SEM micrograph of a starch-based sample**

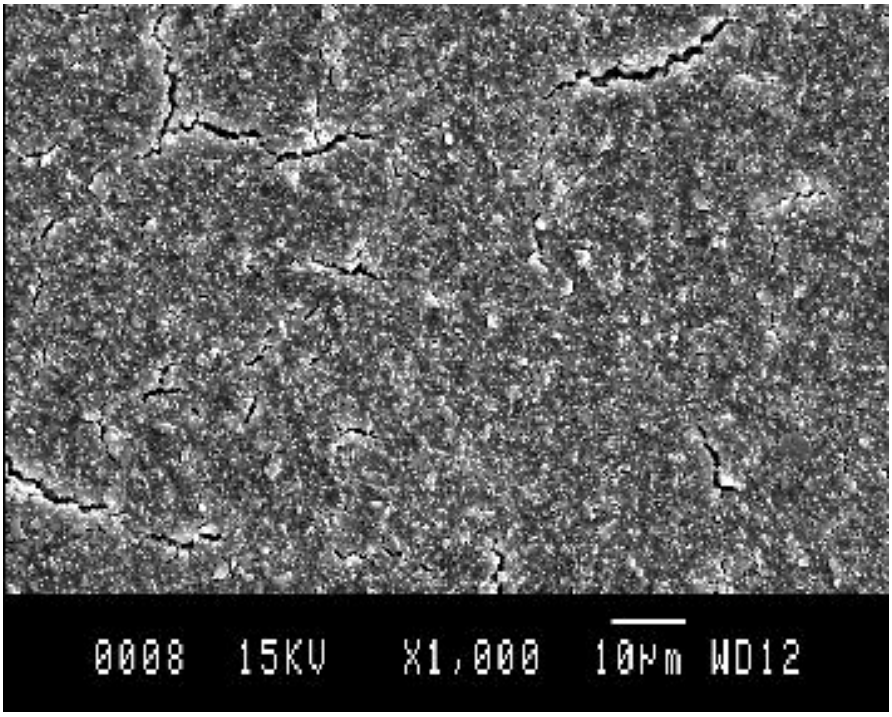


**Figure 9 –SEM micrograph of "mud cracks" on the surface of a low $T_g$ latex-based coating layer**

### *3.3. Pore-Cor*

The values generated by Pore-Cor for our samples are shown in Table 2. The visual representations of two of the simulated structures are shown in figs.10-11.

It is interesting to observe how thinner latex-based coating layer has a lower connectivity and a more random structure; the high $T_g$ rod 2 has a completely random structure, as shown by fig.10 and by its value of correlation level in Table 2. This can once again be interpreted taking into account the diameters of the biggest pigment particles, which are ~ 5 μm, in relation to the thickness of the coating layer. In the case of the thin coating layer, the dimension of the biggest particle is larger or equal to the thickness of the layer; this limits the freedom of movement and rearrangement of the particles while the coating layer is drying, leading to a random structure. If the coating layer is thicker than the biggest particle of calcium carbonate, the structure is free to rearrange and this leads to more order and, therefore, to a higher correlation level.

**Table 2 - Pore-Cor results**

| Sample | Experimental and simulated porosity (%) | Simulated connectivity | Simulated liquid permeability (milliDarcy) | Simulated correlation level |
|---|---|---|---|---|
| Low $T_g$ latex rod 2 | 21.0 | 3.62 | 3.37E-7 | 0.16 |
| Low $T_g$ latex rod 3 | 30.8 | 5.13 | 9.03E-6 | 0.20 |
| High $T_g$ latex rod 2 | 29.2 | 4.03 | 1.52E-6 | 0.03 |

| | | | | |
|---|---|---|---|---|
| High $T_g$ latex rod 3 | 18.9 | 5.56 | 4.31E-7 | 0.31 |
| Starch rod 2 | 13.5 | 5.30 | 6.87E-7 | 0.37 |
| Starch rod 3 | 16.3 | 5.03 | 6.91E-7 | 0.28 |

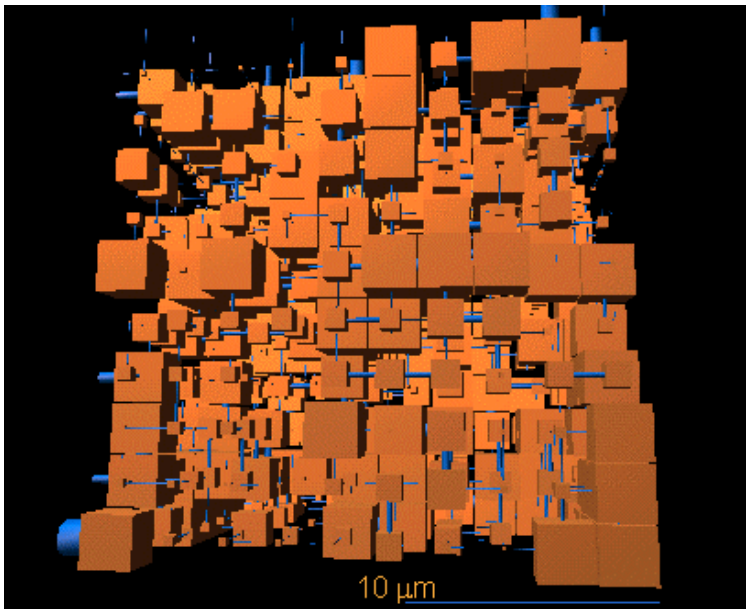


**Figure 10 - modelled structure of high $T_g$ latex-based coating applied with rod 2: the structure results show it to be completely random**

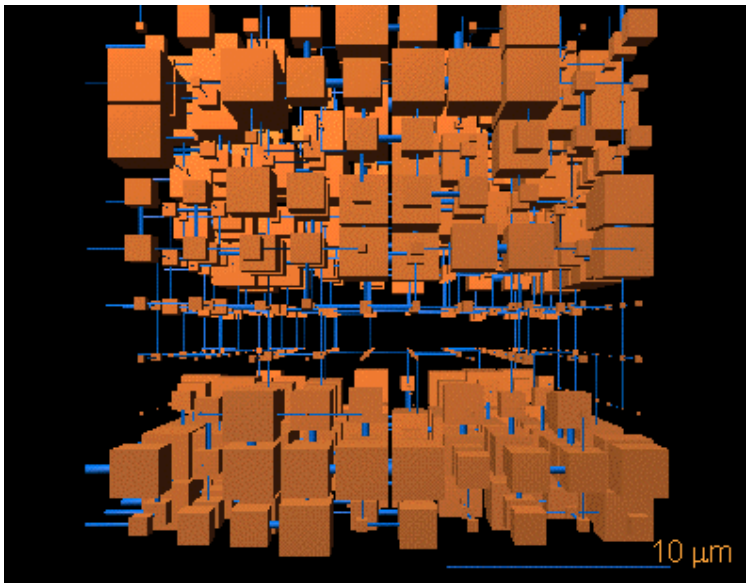


**Figure 11 - modelled structure of high $T_g$ latex-based coating applied with rod 3: showing central zone of small throats and pores.**

Pore-Cor can simulate the behaviour of fluids as these structures dry. The distribution of air as water evaporates is assumed to be the same as if air was a non-wetting fluid displacing the water by percolation. In fig.12 the results of this algorithm applied to the starch-based sample coated with rod 2 are shown, in which the percolation intrusion occurs from above.

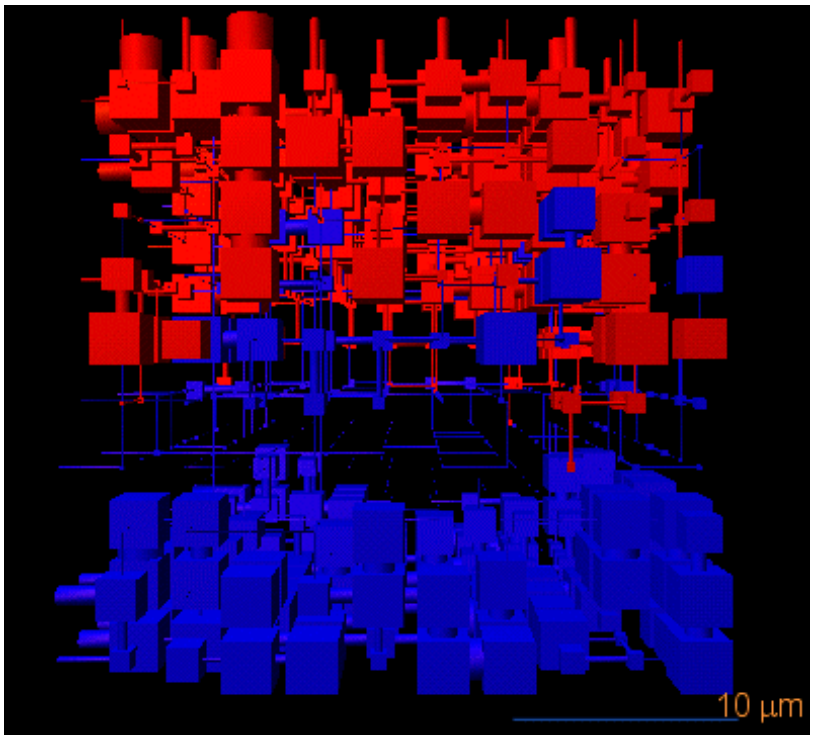


**Figure 12 – simulation of evaporation from the starch-based rod 2 modelled structure using the percolation algorithm (acting from above) of an effective non-wetting fluid to describe the air/water distribution during the evaporation process.**

The subsequent wetting of the dried structure by a wetting fluid can also be simulated using a "wetting algorithm", based on the Bosanquet equation (Schoelkopf et al. [20]). In fig.13 it is possible to observe the flow of water into the structure from above after 1 ms. It is interesting to observe how the water flows deeper into the structure following preferential paths.

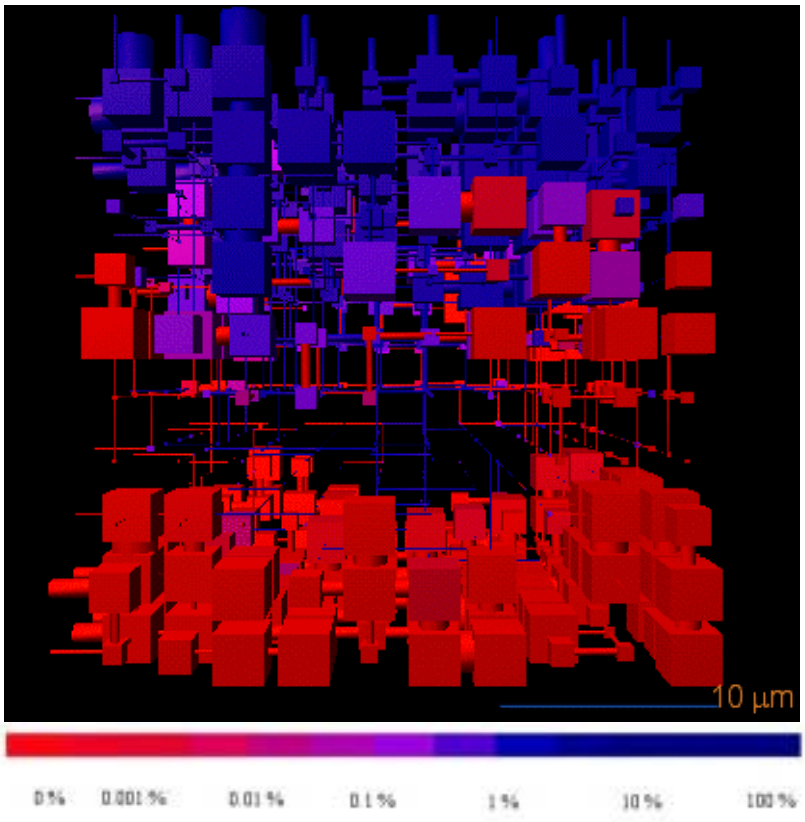


**Figure 13 - simulation of wetting into the starch-based rod 2 modelled structure**

Balancing these wetting and percolation properties can be used to describe the time dependency and rearrangement of fluid in a given porous structure, which will be key to the understanding of evaporative drying and associated shrinkage phenomena.

## 4. Conclusions and future research work

The shrinkage-related behaviour of different binders in a coating colour formulation is a problem well known to the paper-making industry. In this paper, we indirectly quantified the force acting upon drying, and the relative importance of capillary forces and film-forming polymer shrinkage forces. Since the substrate used in our experiments does not absorb water and the dewatering can only take place by

evaporation, the values of the surface forces measured during these experiments may not compare well with the forces acting on coated paper. However, they can give important information about the mechanism of drying for different binders.

The mercury porosimetry analysis on the dried porous structure, formed by the pigment and the binder, showed interesting trends, enabling us to explain the difference in behaviour for the different binders. The Pore-Cor network modelling software package provided model 3D structures representing the porous structures and their pore-level properties. The models indicated that distinctive banding of thin layer structures occurred during drying, in which the middle layers exhibited reduced porosity due to particle rearrangement during shrinkage.

Using these 3D modelled structures with the percolation algorithm used to simulate the mercury intrusion, we aim to simulate in more detail the water evaporation from the porous structure, as shown in fig.12, and its redistribution in the structure itself as a function of time using the wetting algorithm as shown in fig.13. This will finally allow the calculation of the meniscus forces in the simulated network structures and their comparison with the experimental data presented in this paper.

## References


1. J. Watanabe and P. Lepoutre, *J. Appl. Polym. Sci.*, 27, 4207-4219 (1982)

2. S.X. Pan, H.T. Davis and L.E. Scriven, *Tappi J.*, 78, 127-143 (1995)

3. P. Bernada and D. Bruneau, *Tappi J.*, 79, pp. 130-143 (1996)

4. P. Bernada and D. Bruneau, *Drying Technol.*, 15, 2061-2087 (1997)

5. R. Groves, G.P. Matthews, J. Heap, M.D. McInnes, J.E. Penson and C.J. Ridgway, *Proceedings of the 12th Fundamental Research Symposium : Science of Papermaking*, The Pulp and Paper Fundamental Research Society, PITA, 1149-1182, (2001)

6. J.B. Laurindo and M. Prat, *Chem. Eng. Sci.*, 51, 5171-5185 (1996)

7. J.B. Laurindo and M. Prat, *Drying Technol.*, 16, 1769-1787 (1998)

8. J.B. Laurindo and M. Prat, *Chem. Eng. Sci.*, 53, 2257 (1998)

9. C. Gao, *Appl. Phys. Lett.*, 71, 1801-1803 (1997)

10. C. Gao, P. Dai, A. Homola and J. Weiss, *ASME Trans. J. Tribology*, 120, 358-368 (1998)

11. J.C. Husband, "A Comparison of the Interactions of Various Starch Derivatives and Sodium Carboxymethyl Cellulose with Kaolin and Paper Coating Latex Suspensions," Ph.D. Thesis, University of Manchester Institute of Science and Technology (1997)

12. J.C. Husband, *Colloids Surfaces*, A131, 145-159 (1998)

13. R.W. Johnson, L. Abrams, R. Maynard and T.J. Amick, *Tappi J.*, 82, 239-251 (1999)

14. L. Abrams, W. Favorite, J. Capano, and R.W. Johnson, *Proceedings of the 1996 Tappi Coating Conference,* Tappi Press, Atlanta, 185-192 (1996)

15. C.J. Ridgway and P.A.C. Gane, *Nordic Pulp Paper Res. J.* (2002) in press.

16. P.A.C. Gane, J. P. Kettle, G.P. Matthews and C.J. Ridgway, *Ind. Eng. Chem. Res.*, 35, 1753-1764 (1995)

17. J.P. Kettle and G.P. Matthews, *Proceeding of the 1993 Tappi Advanced Coating Fundamentals Symposium,* Tappi Press, Atlanta, 121-126 (1993)

18. C.J, Ridgway, P.A.C. Gane and J. Schoelkopf, *J. Colloid Interface Sci.*, 252, 373-382 (2002)

19. C.J. Ridgway, J. Schoelkopf, G.P. Matthews, P.A.C. Gane and P.W. James, *J. Colloid Interface Sci.,* 239, 417-431 (2001)

20. J. Schoelkopf, C.J. Ridgway, P.A.C. Gane, G.P. Matthews and D.C. Spielmann, *J. Colloid Interface Sci.*, 227, 119-131 (2000)

21. R.T. Frenner, Mechanics of Solids, pp. 314-388, Blackwell Scientific Publications (1989)

# Appendix

## *Beam theory*

The elementary beam theory [21] gives:

$$M = \frac{EI}{R} \qquad \text{(A-1)}$$

where $M$ is the bending moment, $E$ is the elastic modulus, $I$ is the second moment of inertia related to the $z$ axis, $R$ is the radius of curvature of the deformed beam. Equation A-1 is considered valid when the deformed beam is circular.

## *Effect of the coating layer*

It is possible to assume that the coating gives rise to a total surface traction $T$ (fig.14) and, hence, to a bending moment $M=T\cdot d$, where $2d$ is the thickness of the beam. From equation A-1:

$$\frac{EI}{R} = T \cdot d \qquad \text{(A-2)}$$

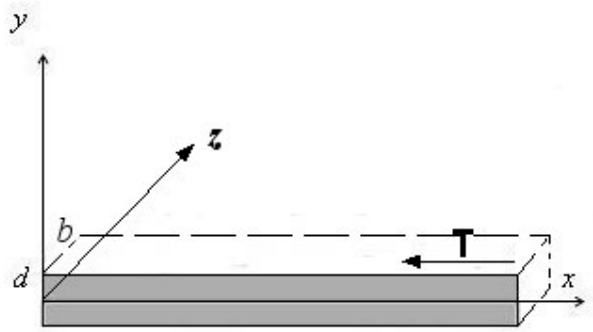


**Figure 14 – beam and traction acting on its surface.**

where $I = b(2d)^3/12$, $b$ is the width of the beam and the product $EI$ is called the "beam stiffness".

## *Radius of curvature of the bending beam*

For a generic function $y = f(x)$ the radius of curvature is

$$\frac{1}{R} = \frac{y''}{\sqrt{1+y'^2}} \qquad \text{(A-3)}$$

where $y' = dy/dx$ and $y'' = d^2y/dx^2$. For small $y'$, $1/R \cong y''$. If we have a circular deformation through $(x_0, y_0)$, then:

$$\frac{1}{R} = \frac{2y_0}{x_0^{\,2} + y_0^{\,2}} \qquad \text{(A-4)}$$

Equations A-3 and A-4 are consistent if $x_0^2 >> y_0^2$, i.e. for small deformation.

If a deflection $y_0$ is measured, substituting from equation A-2:

$$T \cdot d = \frac{2EIy_0}{x_0^{\,2} + y_0^{\,2}} \qquad \text{(A-5)}$$

If $x_0$, $y_0$ and $EI$ are known, $T$ can be calculated from equation A-5. The stress acting on the surface of the beam can be calculated as $\tau = T / b \cdot x_0$.

Since $T \propto I \propto b$, the stress $\tau$ is independent of the strip width $b$.

## *Evaluation of the stiffness of the beam EI*

The standard beam theory is also helpful if the stiffness of the beam is unknown. Performing a simple experiment (figure 15) and measuring the deflection of the strip due to its own weight (which is negligible when compared to the stress caused by the drying coating layer, but enough to cause a small deflection), it is possible to determine the value of the product $EI$.

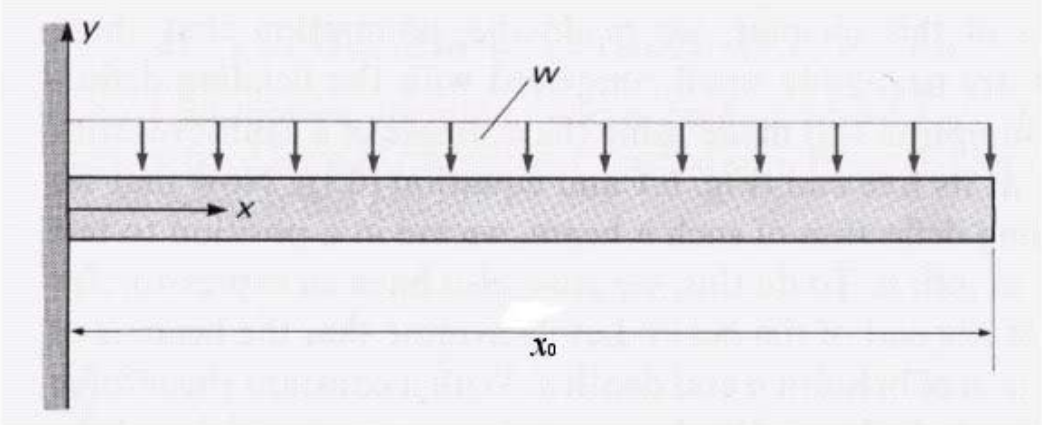


**Figure 15: beam with uniformly distributed weight. The deflection of the beam due to its own weight can be used to calculate *EI***

Let us call *w* the weight per unit of length and setting $1/R \cong y''$ equation A-1 gives:

$$EI\frac{\mathrm{d}^4 y}{\mathrm{d}x^4} = -w \qquad \text{(A-6)}$$

$$\therefore \quad EI \cdot y(x) = -\frac{w \cdot x^4}{24} + \frac{w \cdot x_0 \cdot x^3}{6} - \frac{w \cdot x_0^2 \cdot x^2}{4} + A \cdot x + B \qquad \text{(A-7)}$$

The boundary conditions are:

$$y(0) = y'(0) = 0$$

This leads to:

$$y(x) = \frac{1}{EI}\left\{-\frac{w}{24}\left(x^4 + 6x_0{}^2 \cdot x^2 - 4x_0 \cdot x^3\right)\right\} \qquad \text{(A-9)}$$

For $x = x_0$, equation A-9 becomes:

$$y_1 = y(x_0) = \frac{1}{EI}\left(-\frac{3x_0^4 \cdot w}{24}\right) = -\frac{x_0^4 \cdot w}{8EI} \qquad \text{(A-10)}$$

And finally:

$$EI = -\frac{w \cdot {x_0}^4}{8 y_1} \qquad \text{(A-11)}$$